

Photocatalytic O₂ oxidation of CH₄ to CH₃OH on AuFe-ZnO bifunctional catalyst

Haoran Du^a, Xiuping Li^a, Zhiyang Cao^a, Shao Zhang^a, Wenzhao Yu^a, Fengyu Sun^a, Shengyao Wang^b, Jingjing Zhao^a, Jiaqi Wang^a, Yuan Bai^a, Juanjuan Yang^a, Ping Yang^a, Bo Jiang^{a,*}, Hexing Li^{a,*}

^a The Education Ministry Key Lab of Resource Chemistry, Joint International Research Laboratory of Resource Chemistry, Shanghai Key Laboratory of Rare Earth Functional Materials, Shanghai Frontiers Science Center of Biomimetic Catalysis, College of Chemistry and Materials Science, Shanghai Normal University, Shanghai 200234, PR China

^b College of Science, Huazhong Agricultural University, Wuhan 430070, PR China



ARTICLE INFO

Keywords:

AuFe-ZnO bifunctional catalyst
Selective CH₄ oxidation by O₂ to CH₃OH
Photocatalytic generation of H₂O₂
Fenton-like reaction

ABSTRACT

Selective oxidation of CH₄ by O₂ to produce CH₃OH under mild reaction conditions is of importance but remains a significant challenge. Herein, we report a novel nanocomposite of highly dispersed Au and Fe species on ZnO (AuFe-ZnO). During photocatalytic O₂ oxidation of CH₄ to CH₃OH, this AuFe-ZnO acts as a bifunctional catalyst to drive one-pot cascade reactions (O₂ + H₂O → H₂O₂ and CH₄ + H₂O₂ → CH₃OH + H₂O). The ZnO semiconductor generates electrons under irradiation to produce H₂O₂ from O₂, in which the photo-induced holes could activate CH₄ to form •CH₃. The Au served as a co-catalyst for activating CH₄, while the Fe²⁺ species catalyzed Fenton-like reactions by activating H₂O₂ to form •OH radicals, followed by reacting with •CH₃ to produce CH₃OH. The synergistic effects of Au, Fe, and ZnO result in a high CH₃OH yield of 1365 μmol·g⁻¹·h⁻¹ with high CH₃OH selectivity of up to 90.7%.

1. Introduction

CH₄ has been widely used as fossil energy as the principal constituent of natural gas [1–3]. However, CH₄ combustion releases a great number of CO₂. Both CO₂ and CH₄ are strong green-house effecting gases [4,5]. With the rapid development of non-fossil energy, instead of combustion, the CH₄ conversion into valuable chemical products like CH₃OH becomes more and more important [6–8]. However, most CH₄ conversion reactions require harsh conditions due to the stable molecule structure, leading to high energy consumption and low selectivity toward target products as well as difficult operation [9–12]. The mature industrial route is an energy-intensive two-stage process involving the manufacture of synthesis gas through steam or dry reforming and subsequent Fischer-Tropsch synthesis [9,12–14]. Those reactions usually perform at 700–800 °C, which inevitably causes the deactivation of catalysts and high energy consumption. Recently, selective oxidation of CH₄ under mild conditions has caused increasing attention owing to the energy-saving, easy operation, and environmental friendliness [15–21]. For example, Hutchings et al. reported that the Au-Pd catalyst exhibited

high selectivity to CH₃OH during CH₄ oxidation by H₂O₂ at 50 °C [9]. But, their practical applications are still quite limited by the use of costly oxidants or corrosive reaction media, e.g., selenic acid [22], oleum [23], and H₂O₂ [24,25].

Photocatalytic selective O₂ oxidation of CH₄ represents a promising way for CH₄ conversion owing to the mild reaction conditions, low price of O₂, environmental-friendly and energy-saving process [17–21]. Typical semiconductors, including WO₃ [10,19,26], TiO₂ [17,27–29], ZnO [20,30–32], C₃N₄ [33], and BiOCl [34] have been selected as potential candidates to drive photocatalytic CH₄ conversion. For instance, noble metal modified-ZnO photocatalysts displayed high activity in water-medium photocatalytic O₂ oxidation of CH₄ [31]. The holes generated from light-exciting semiconductors play the dominant role in breaking the C-H bond of CH₄ to form •CH₃ radicals, followed by reacting with •OH to produce CH₃OH. However, the photoelectrons may react with O₂ to generate O₂•⁻ radicals, which can react directly with •CH₃ and/or the as-produced CH₃OH to produce CH₃OOH, CO, and CO₂ [33], leading to the poor selectivity to CH₃OH (< 30%). Both the experimental results and theoretical prediction demonstrated that the

* Corresponding authors.

E-mail addresses: Jiangbo@shnu.edu.cn (B. Jiang), Hexing-Li@shnu.edu.cn (H. Li).

H_2O_2 -assistant photocatalytic CH_4 oxidation could enhance the selectivity to CH_3OH owing to the formation of more $\bullet\text{OH}$ radicals [18,21]. For example, the photocatalytic H_2O_2 oxidation of CH_4 on $\text{FeO}_x/\text{TiO}_2$ in an aqueous solution exhibited nearly 90% CH_3OH selectivity under ambient conditions [21]. Wang et al. also reported a Fenton-like reaction for H_2O_2 oxidation of CH_4 with high selectivity to CH_3OH on the $\text{FeOOH}/\text{Li}_{0.1}\text{WO}_3$ [35]. However, all those reactions need the addition of H_2O_2 oxidant, leading to the enhanced cost. Meanwhile, those reactions also displayed low activity due to the difficult activation of H_2O_2 into $\bullet\text{OH}$ radicals, corresponding to the low CH_3OH selectivity and yield.

Herein, we reported a novel bifunctional AuFe-ZnO catalyst comprised of Au nanoparticles and $\text{Fe}^{2+}/\text{Fe}^{3+}$ species well dispersed on the ZnO . The Au acted as both the electron transfer conductor and the co-catalyst to promote photocatalytic production of H_2O_2 from O_2 under Xe lamp irradiation, together with the activation of CH_4 into $\bullet\text{CH}_3$. While, the Fe^{2+} species activated H_2O_2 into $\bullet\text{OH}$, followed by reacting with $\bullet\text{CH}_3$ to form the target product CH_3OH . The as-resulted Fe^{3+} could be reduced by photoelectrons, leading to the cycling Fenton-like reactions. The synergistic effects of the AuFe-ZnO catalyst during one-pot cascade photocatalytic reactions and Fenton-like reactions greatly enhanced the efficiency during photocatalytic O_2 oxidation of CH_4 at 20°C, corresponding to the CH_3OH yield of $1365 \mu\text{mol}\cdot\text{g}^{-1}\cdot\text{h}^{-1}$ with the CH_3OH selectivity up to 90.7%.

2. Experimental

2.1. Catalyst preparation

2.1.1. Preparation of Au-ZnO

The Au-ZnO photocatalyst was prepared by a modified deposition-precipitation method. Firstly, 500 mg ZnO was dispersed in 50 mL HAuCl_4 aqueous solution containing the desired amount of Au at pH = 9 adjusted with 0.20 M NaOH. The mixture was vigorously stirred for 2 h at 80°C. After being cooled to 25°C, the solid was separated by centrifugation and thoroughly washed with water. After being dried at 80°C for 12 h, it was heated at a ramping rate of 5 °C/min to 200°C and kept at this temperature for 2 h. The as-prepared sample was denoted as Au_xZnO , where x represents the Au loading in weight percentage (wt%).

2.1.2. Preparation of Fe-ZnO

A highly reproducible impregnation method was used to prepare modified ZnO photocatalysts. Briefly, a certain amount of FeCl_2 was dissolved in 50 mL of deionized water containing 500 mg ZnO . The mixture was vigorously stirred for 2 h at 80°C. After being cooled to 25°C, the solid was separated by centrifugation and thoroughly washed with water. After being dried at 80°C for 12 h, it was heated at a ramping rate of 5°C·min⁻¹ to 200°C and kept at this temperature for 2 h. The as-received sample was denoted as $\text{Fe}_y\text{-ZnO}$, where y refers to the Fe loading in weight percent (wt%).

2.1.3. Preparation of AuFe-ZnO

The AuFe-ZnO photocatalyst was prepared by the same method for preparing Au-ZnO except for replacing ZnO with Fe-ZnO . The as-obtained photocatalyst was denoted as $\text{Au}_x\text{Fe}_y\text{-ZnO}$, where x and y refer to the weight percentage (wt%) of Au and Fe loadings, respectively. For comparison, the $\text{Au}_{1.0}\text{Fe}_{0.33}\text{-ZnO}$ was also calcined at 400°C for 2 h and 12 h, respectively.

2.2. Characterization

The morphologies were characterized by transmission electron microscope (TEM, JEM-2010, Japan). The crystalline structure was analyzed by X-ray diffraction pattern (XRD) with Cu K α radiation (Bruker advance D8, Germany), and the data was recorded at a scan rate of 5 min⁻¹. The N₂ adsorption-desorption isotherms were obtained at 77

K using a Micromeritics ASAP 2010 instrument, based on which the specific surface area (S_{BET}) and pore volume (V_p) were calculated by applying Brunauer-Emmett-Teller (BET) and Barrett-Joyner-Halenda (BJH) models. The chemical state for surface elements was characterized by X-Ray photoelectron spectroscopy (XPS) on an ESCLAB250 spectrometer, using a monochromatic Al K α radiation source. All the binding energies (BEs) were calibrated using the C1s peak at 284.8 eV as a reference. Electron paramagnetic resonance (EPR) spectroscopy measurement was performed on a Bruker ESP A300 spectrometer, using 5, 5-dimethyl-1-pyrroline-N-oxide (DMPO) to monitor hydroxyl radicals. The light absorbance was detected on the ultraviolet-visible diffuse reflectance spectroscopy (UV-vis DRS, Shimadzu UV-2450) with high-purity BaSO_4 as a standard reagent for baseline calibration. According to the UV-vis diagram, the corresponding band gap energy is calculated by the Kubelka-Munk equation:

$$\alpha h\nu = A(h\nu - E_g)^n$$

Where A, E_g , v, h, and α represent the constant, band gap, optical frequency, Planck constant, and absorption coefficient, respectively. n is equal to 1/2 or 2 corresponding to the indirect band gap or direct band gap of the semiconductor. All the photoelectron-chemical performance tests were carried out in Shanghai Chenhua CHI760E electrochemical workstation using a three-electrode system, using FTO glass coated with the photocatalyst as the working electrode, platinum plate as the counter electrode, Ag/AgCl electrode as the reference electrode, and 0.50 M Na_2SO_4 solution as electrolyte. The photoelectron-hole recombination was analyzed on a fluorometer (PL, Cony Eclipse, Varian, USA) with an excitation wavelength of 348 nm. The surface adsorption of intermediates during the reaction process was observed through the in situ Fourier transform infrared spectroscopy (FT-IR) on a Nicolet iS10 spectrometer (Thermo Scientific) equipped with an in situ reaction chamber.

2.3. Activity test

The photocatalytic reactions were conducted in a 100 mL autoclave equipped with a quartz window to allow light irradiation (See **Scheme S1** in **Supporting Information**). Typically, 40 mg photocatalyst was dispersed in 20 mL water by ultrasonication for 2 min. Then, the mixture was added to the glass liner in the autoclave. After purging with O_2 several times to exhaust air, the reactor was filled with 2 bar O_2 and 18 bar CH_4 . The photocatalytic reaction was then started by a 300 W Xe lamp irradiation at 20°C under 600 rpm stirring. After the reaction, the mixture was cooled down to 10°C. The gas products (CH_4 , C_2H_6 , C_2H_4 , C_2H_2 , H_2 , CO, CO_2) were analyzed by gas chromatography (GC 7890B, Agilent, after referred to as GC1) equipped with flame ionization detector (FID) fixed with a HP-PLOT/Q column (30 m × 0.5 mm) and a thermal conductivity detector (TCD) connected to TDX-01 column (1 m × 1/8). The liquid products (CH_3OH , $\text{CH}_3\text{CH}_2\text{OH}$, CH_3COOH , HCOOH , $\text{CH}_3\text{CH}_2\text{OH}$, CH_3COCH_3 , HCHO , etc.) were collected by filtration, followed by analyzing with a chromatography (GC 7890B, Agilent, after referred to as GC2) equipped with flame ionization detectors (FID) fixed a HP-FFAT column (50 m × 0.2 mm) and high-performance liquid chromatography (HPLC, Agilent) equipped with an ultraviolet-visible detector (UVD) set with a Hi-Plex H column (7.7 × 300 mm) as well as acetylacetone color-developing method. The CH_3OOH was analyzed by the ¹H nuclear magnetic resonance (NMR) spectroscopy immediately after the reaction to avoid its decomposition (Fig. S1).

The CH_3OH yield was calculated according to the following equation:

$$\text{CH}_3\text{OH Yield} (\mu\text{mol} \cdot \text{g}^{-1} \cdot \text{h}^{-1}) = n_{\text{CH}_3\text{OH}} / (m_{\text{catalyst}} \cdot t)$$

Where $n_{\text{CH}_3\text{OH}}$ represents the micromoles of CH_3OH produced during the CH_4 oxidation reaction, while m_{catalyst} and t refer to the catalyst mass (g) and the reaction time (h), respectively. The yields of other products were

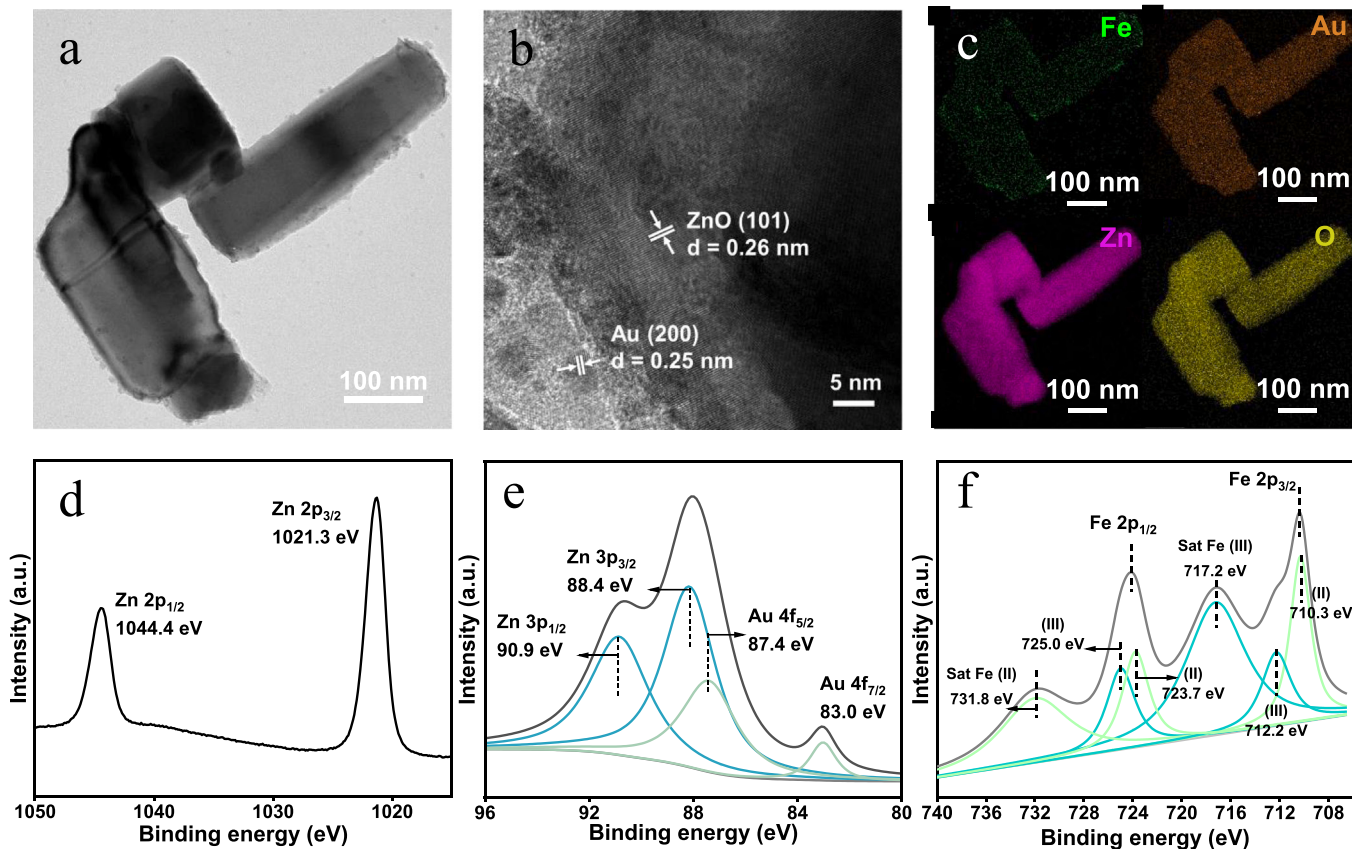


Fig. 1. (a) TEM and (b) HR-TEM images, as well as (c) element mappings of $\text{Au}_{1.0}\text{Fe}_{0.33}\text{-ZnO}$. XPS spectra at (d) Zn 2p, (e) Au 4f, (f) Fe 2p levels in $\text{Au}_{1.0}\text{Fe}_{0.33}\text{-ZnO}$.

calculated in similar equations.

The CH_3OH selectivity was calculated according to the following equation:

$$\begin{aligned} \text{CH}_3\text{OH Selectivity}(\%) = & [n_{\text{CH}_3\text{OH}} / (n_{\text{CH}_3\text{OH}} + n_{\text{CH}_3\text{OOH}} + n_{\text{HCHO}} \\ & + n_{\text{HCOOH}} + n_{\text{CO}_2} + n_{\text{CO}})] \times 100\% \end{aligned}$$

where $n_{\text{CH}_3\text{OH}}$, $n_{\text{CH}_3\text{OOH}}$, n_{HCHO} , n_{HCOOH} , n_{CO_2} , n_{CO} represent the microoles of CH_3OH , CH_3OOH , HCHO, HCOOH, CO_2 and CO produced during CH_4 oxidation reaction.

In the recycling test, the $\text{Au}_{1.0}\text{Fe}_{0.33}\text{-ZnO}$ was separated after each reaction, followed by washing and drying at 90°C for 2 h to remove all adsorbed organic pollutants and solvent. Then, the next cycle of photocatalytic reaction was performed under the same reaction conditions.

3. Results and discussion

3.1. Structural characteristics

The actual Au- and Fe-contents were determined by ICP (see Table S1). As shown in Fig. 1a, the TEM image displayed nanosized polygons of the $\text{Au}_{1.0}\text{Fe}_{0.33}\text{-ZnO}$, almost the same as those of ZnO , $\text{Au}_{1.0}\text{-ZnO}$, $\text{Fe}_{0.33}\text{-ZnO}$ (see Fig. S2). The enlarged TEM images and the corresponding particle size distribution curves (Fig. S3) demonstrated the Au in the $\text{Au}_{1.0}\text{Fe}_{0.33}\text{-ZnO}$ was present in nanoparticles with the average size around 4.7 nm and the increase in either the calcination temperature or the calcination time caused significant increase in Au nanoparticle size. Meanwhile, the XRD patterns (Fig. S4) revealed that all the $\text{Au}_{1.0}\text{Fe}_{0.33}\text{-ZnO}$, $\text{Au}_{1.0}\text{-ZnO}$, and $\text{Fe}_{0.33}\text{-ZnO}$ exhibited only the same diffractional peaks as observed in pure ZnO , corresponding to the hexagonal wurtzite structure of ZnO (PDF#36–1451). No significant diffractional peaks characteristic of Au and Fe were observed owing to their high dispersion and low contents. In addition, all the ZnO , $\text{Au}_{1.0}\text{Fe}_{0.33}\text{-ZnO}$,

$\text{Au}_{1.0}\text{-ZnO}$, and $\text{Fe}_{0.33}\text{-ZnO}$ exhibited similar II-type N_2 adsorption-desorption isotherms (see Fig. S5), together with the similar specific surface area (S_{BET}), pore diameter (D_p) and pore volume (V_p) calculated based on the BJH and BET methods (see Table S2). After Fe-doping, the S_{BET} slightly increased, while both the D_p and the V_p slightly decreased, possibly due to the presence of a new porous structure constructed by Fe species. Those results demonstrated that the deposition of Au and Fe and Au/Fe onto ZnO had little influence on the original morphology, crystalline structure, and textural parameters. The HRTEM image of $\text{Au}_{1.0}\text{Fe}_{0.33}\text{-ZnO}$ (Fig. 1b) clearly showed the lattice spacing of 0.25 nm and 0.26 nm, which corresponds to the (200) facet of Au and the (101) facet of ZnO , respectively. However, no significant Fe species were observed, probably due to the low content and the high dispersion. The Elemental Mappings (EDS) in Fig. 1c displayed the uniform distribution of Au and Fe onto the ZnO support. The XPS spectra revealed that all the Zn species in the $\text{Au}_{1.0}\text{Fe}_{0.33}\text{-ZnO}$ were present in Zn^{2+} state, corresponding to two peaks with the bind energies of 1044.4 and 1021.3 eV at $2p_{1/2}$ and $2p_{3/2}$ levels respectively and 90.9 and 88.4 eV at $3p_{1/2}$ and $3p_{3/2}$ levels, respectively (Fig. 1d). All the Au species were present in the metallic state, corresponding to the binding energy of 87.4 and 83.0 eV at $4f_{5/2}$ and $4f_{7/2}$ levels, respectively (Fig. 1e). The Fe species were present in both the Fe^{2+} and Fe^{3+} states (Fig. 1f). The peaks with binding energies of 712.2 and 725.0 eV, together with a robust satellite signal at 717.2 eV, could be assigned to Fe^{3+} [36–38], while the peaks located at 710.3 and 723.7 eV, together with a strong shakeup satellite at 731.8 eV, corresponded to Fe^{2+} state [37,38].

The UV-vis DRS spectra (Fig. S6a) revealed that the pure ZnO presented only light absorbance in UV area with the wide band gap (E_g) around 3.24 eV as calculated from the plot of Kubelka-Munk function versus photon energy (see Fig. S6b), suggesting that ZnO could be excited only by UV lights due to its energy band gap. All the $\text{Au}_{1.0}\text{Fe}_{0.33}\text{-ZnO}$, $\text{Au}_{1.0}\text{-ZnO}$, and $\text{Fe}_{0.33}\text{-ZnO}$ exhibited similar light absorptions in

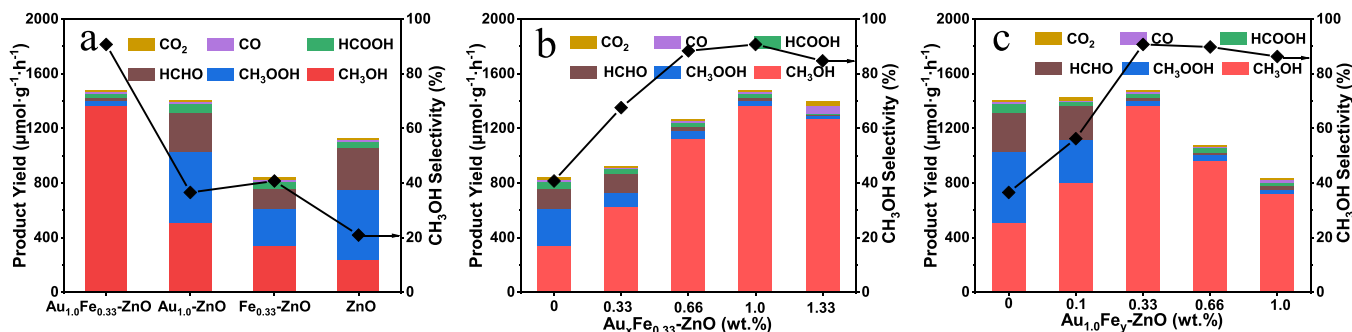


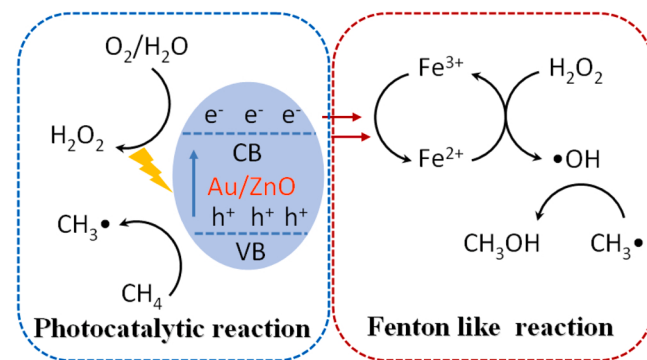
Fig. 2. Performances of different photocatalysts in CH₃OH oxidation by changing (a) photocatalysts, (b) the Au-content in Au_xFe_{0.33}-ZnO, and (c) the Fe-content in Au_{1.0}Fe_y-ZnO. Reaction conditions: 40 mg catalyst, 20 mL H₂O, 2.0 bar O₂, 18 bar CH₄, 20°C reaction temperature, 1 h reaction period, stirring rate 500 rpm, 300 W Xe lamp irradiation.

UV area to pure ZnO, with the same Eg values. Those results demonstrated all the Au_{1.0}Fe_{0.33}-ZnO, Au_{1.0}-ZnO and Fe_{0.33}-ZnO were UV photocatalysts like ZnO. The photocurrent response curves obtained under Xe lamp irradiation (Fig. S7a) demonstrated that the pure ZnO exhibited very low photocurrent density. Loading Au, Fe, and AuFe gradually increased the photocurrent density. The PL spectra obtained under 348 nm excitation (Fig. S7b) indicated that depositing Au, Fe and AuFe caused a gradual decrease in density of the peak around 500 nm, implying the decrease in the photoelectron-hole recombination probability. Furthermore, the EIS spectra (Fig. S7c) revealed that the arc radius became smaller by loading Au onto ZnO, corresponding to the enhanced rate of electron transfer which could be attributed to the good electric conductivity of metallic Au. The rapid electron transfer could facilitate the separation of photoelectrons from holes, corresponding to the lower photoelectron-hole recombination. Therefore, because of the similar UV light harvesting ability in almost the same region, the Au_{1.0}-ZnO and Fe_{0.33}-ZnO exhibited stronger photocurrent density than the pure ZnO, mainly owing to the inhibition of photoelectron-hole recombination by facilitating electron transfer or constructing heterojunctions. The Au_{1.0}Fe_{0.33}-ZnO exhibited the strongest photocurrent density owing to the synergistic effects from both Au and Fe species.

3.2. Catalytic performance

The photocatalytic CH₄ oxidation by gas O₂ was examined in a 100 mL autoclave with a quartz window for light irradiation (see the experimental details and the picture in the Supporting Information). Fig. 2a demonstrated that the pure ZnO, Au_{1.0}-ZnO, and Fe_{0.33}-ZnO photocatalysts displayed poor CH₃OH selectivity and yield due to the rapid formation of HCHO and CH₃OOH during photocatalytic O₂ oxidation of CH₄ under present reaction conditions. However, photocatalytic CH₄ oxidation on the Au_{1.0}Fe_{0.33}-ZnO resulted in the target CH₃OH. The main byproducts were CH₃OOH and HCHO, suggesting that cooperation between Au and Fe on the ZnO could remarkably promote CH₃OH production and efficiently inhibit either CH₃OOH or HCHO production. Only trace of HCOOH, CO, and CO₂ byproducts was detected. Both the CH₃OH selectivity and the CH₃OH yield increased with the increase of either the Au-content in Au_xFe_{0.33}-ZnO or the Fe-content in Au_{1.0}Fe_y-ZnO. The optimum catalyst was determined as Au_{1.0}Fe_{0.33}-ZnO, corresponding to 1.0 wt% Au and 0.33 wt% Fe on the ZnO. Further increase in the Au-content caused slightly decrease in both the CH₃OH selectivity and the CH₃OH yield (see Fig. 2b). Unlike Au, the further increase of Fe-content resulted in a rapid decrease in CH₃OH yield, but the CH₃OH selectivity remained almost constant (see Fig. 2c).

Because either the Au-content or the Fe-content had little effect on the morphology, the crystalline degree and structural parameters of Au_xFe_y-ZnO, the change of the CH₃OH selectivity and yield could be mainly accounted by considering the coupled photocatalytic reactions and Fenton-like reactions. As briefly illustrated in Scheme 1, the ZnO



Scheme 1. Illustration of one-pot cascade photocatalytic reaction and Fenton-like reaction.

excited by UV-light irradiation to generate photoelectrons and holes. The photoelectrons reduced O₂ to produce H₂O₂ and the photo-induced holes activated CH₄ molecules to form •CH₃ radicals. The Fe²⁺ species on ZnO activated H₂O₂ to form •OH radicals, followed by reacting with •CH₃ to produce target product CH₃OH. The as-resulted Fe³⁺ species could be reduced into Fe²⁺ by photoelectrons, leading to the cycling Fenton-like reactions. Because the photo-induced holes also activated O₂ into O₂^{•-} radicals, which could directly react with •CH₃ to form CH₃OOH and HCHO. In addition, the deep oxidation of CH₃OOH and HCHO by either the O₂^{•-} radicals or the photo-induced holes resulted in the formation of trace byproducts, including HCOOH, CO, and CO₂. The pure ZnO displayed very activity in the photocatalytic production of H₂O₂ and activation of CH₄ molecules to •CH₃. Meanwhile, it also displayed low selectivity to CH₃OH due to the low concentration of •OH radicals in comparison with the O₂^{•-} radicals since only trace H₂O₂ were present, and it was difficult to be activated into •OH radicals in the absence of Fe²⁺ species. Therefore, the ZnO exhibited very low CH₃OH yield during photocatalytic CH₄ oxidation. Depositing Au nanoparticles onto ZnO could significantly enhance the photocatalytic activity in generating H₂O₂ since metallic Au could act as a good electron conductivity for rapid electron transfer to inhibit photoelectron-hole recombination.

Meanwhile, the Au could also act as a co-catalyst to activate CH₄ molecules to form •CH₃. Therefore, the Au_{1.0}-ZnO exhibited a much higher CH₃OH yield than the pure ZnO. However, only a slight increase in the selectivity was observed on the Au_{1.0}-ZnO since the H₂O₂ could not be efficiently activated into •OH radicals in the absence of Fe²⁺ species to react with •CH₃ for producing CH₃OH. A lot of •CH₃ could react with O₂^{•-} to produce CH₃OOH and HCHO as well as other byproducts by deep oxidation [30,32], leading to the poor selectivity to CH₃OOH. Meanwhile, the Fe_{0.33}-ZnO exhibited poor CH₃OH yield because of the insufficient photocatalytic activity in generating H₂O₂.

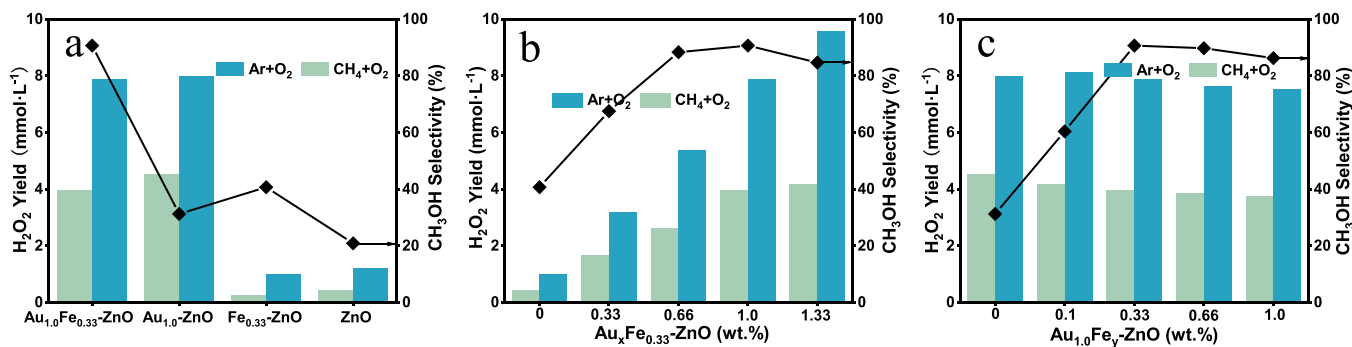


Fig. 3. Corresponding relationship of photocatalytic H_2O_2 generation and activation to the CH_3OH selectivity during CH_4 oxidation in Ar/O_2 or CH_4/O_2 systems by verifying (a) photocatalysts, (b) the Au-content in $\text{Au}_x\text{Fe}_{0.33}\text{-ZnO}$, and (c) the Au-contents in $\text{Au}_{1.0}\text{Fe}_y\text{-ZnO}$. Reaction conditions are given in Fig. 2.

and $\bullet\text{CH}_3$ due to the rapid photoelectron-hole recombination in the absence of Au. The $\text{Fe}_{0.33}\text{-ZnO}$ also exhibited low selectivity to CH_3OH since no enough $\bullet\text{OH}$ radicals could be produced by Fe^{2+} species due to the very low content of H_2O_2 . Therefore, a lot of $\bullet\text{CH}_3$ could react with $\text{O}_2\bullet^-$ to produce CH_3OOH and HCHO , together with the deep oxidation by $\text{O}_2\bullet^-$ to produce HCOOH , CO , and CO_2 byproducts. The highest CH_3OH yield ($1365 \mu\text{mol}\cdot\text{g}^{-1}\cdot\text{h}^{-1}$) and selectivity (90.7%) were achieved on the $\text{Au}_{1.0}\text{Fe}_{0.33}\text{-ZnO}$, obviously owing to the cooperation between the Au-promoted ZnO photocatalytic reaction and Fe-started Fenton-like reaction. The increased Au-content on the $\text{Fe}_{0.33}\text{-ZnO}$ resulted in the rapid formation of H_2O_2 and $\bullet\text{CH}_3$ by photocatalytic reactions. The H_2O_2 could be in situ activated by Fe^{2+} to generate $\bullet\text{OH}$ radicals, followed by reacting with $\bullet\text{CH}_3$ to produce the target product CH_3OH . However, at very high Au-content (1.0 wt%), the CH_3OH yield declined slightly due to the decreased selectivity to CH_3OH since the H_2O_2 could not be rapidly activated into $\bullet\text{OH}$ radicals. Excess $\bullet\text{CH}_3$ could be oxidized by $\text{O}_2\bullet^-$ to produce CH_3OOH and HCHO , followed by deep oxidation on the Au catalyst to form a large amount of CO byproduct. Similarly, the increased Fe-content on the $\text{Au}_{1.0}\text{-ZnO}$ also greatly enhanced CH_3OH yield since incorporating Fe oxides with ZnO could inhibit photoelectron-hole recombination by forming heterojunctions, leading to enhanced photocatalytic activity. Meanwhile, more Fe species could be used for activating H_2O_2 into $\bullet\text{OH}$ radicals, followed by reacting with $\bullet\text{CH}_3$ to form CH_3OH , leading to increased CH_3OH selectivity. Further increase in Fe-content (0.33 wt%) would be harmful to the CH_3OH yield, obviously due to the decrease in activity since the CH_3OH selectivity remained almost unchanged. A possible explanation is the light shielding effect of Fe species on the ZnO photocatalyst at high Fe-content.

To understand the roles of Au and Fe species during selective photocatalytic oxidation of CH_4 with O_2 , the corresponding relationship of H_2O_2 generation to the CH_3OH selectivity was investigated. As shown in

Fig. 3a, the ZnO and $\text{Fe}_{0.33}\text{-ZnO}$ displayed very low and similar H_2O_2 yield, indicating that the Fe species deposited on ZnO played very limited role in promoting H_2O_2 formation. Although both the $\text{Au}_{1.0}\text{-ZnO}$ and $\text{Au}_{1.0}\text{Fe}_{0.33}\text{-ZnO}$ could produce a high concentration of H_2O_2 , the $\text{Au}_{1.0}\text{-ZnO}$ still exhibited much lower CH_3OH selectivity than the $\text{Au}_{1.0}\text{Fe}_{0.33}\text{-ZnO}$ since the H_2O_2 could not efficiently activate into $\bullet\text{OH}$ radicals in the absence of Fe species, corresponding to the low consumption of H_2O_2 in the presence of CH_4 . Thus, the excess $\bullet\text{CH}_3$, which was also generated from photocatalytic reactions, could be oxidized by $\text{O}_2\bullet^-$ radicals to CH_3OOH , HCHO , and CO byproducts due to the deep oxidation. Fig. 3b revealed that the H_2O_2 yield increased linearly with the increasing Au-content in the $\text{Au}_x\text{Fe}_{0.33}\text{-ZnO}$ owing to the enhanced photocatalytic activity in producing both the H_2O_2 and the $\bullet\text{CH}_3$. The maximum CH_3OH selectivity was obtained at an Au-content of 1.0 wt%. Further increase in the Au-content resulted in a slight decrease in the CH_3OH selectivity, though the H_2O_2 yield increased. This could be accounted by considering the limited Fe species, which could effectively activate the as-produced H_2O_2 at high concentration into $\bullet\text{OH}$ radicals, corresponding to the low consumption of H_2O_2 in the presence of CH_4 . Thus, partial $\bullet\text{CH}_3$ could react with $\text{O}_2\bullet^-$ radicals to produce CH_3OOH and HCHO as well as CO byproducts due to the deep oxidation. Fig. 3c demonstrated that, with the increased Fe-content in $\text{Au}_{1.0}\text{Fe}_y\text{-ZnO}$, the H_2O_2 yield generated from photocatalytic reactions remained almost constant. However, the CH_3OH selectivity first increased owing to the enhanced efficiency for activating H_2O_2 into $\bullet\text{OH}$ radicals by Fe species, corresponding to the improved consumption of H_2O_2 in the presence of CH_4 . The maximum efficiency for activating H_2O_2 into $\bullet\text{OH}$ radicals was achieved at the Fe-content of 0.33 wt%. Further increasing of the Fe-content resulted in a decrease in CH_3OH selectivity due to the decreased H_2O_2 yield.

Fig. 4a demonstrated that, on the $\text{Au}_{1.0}\text{Fe}_{0.33}\text{-ZnO}$ photocatalyst, increasing CH_4 pressure caused a rapid increase of CH_3OH yield owing

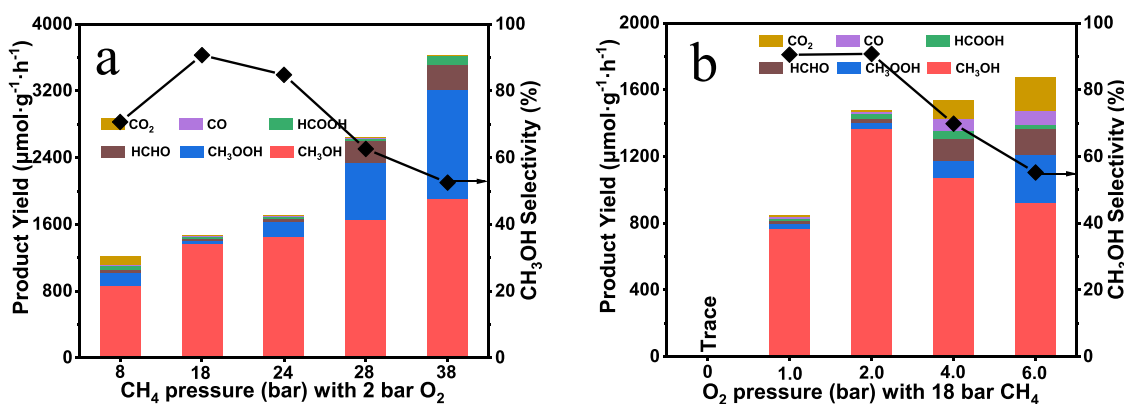


Fig. 4. Effects of (a) CH_4 and (b) O_2 partial pressure on the CH_3OH yield and selectivity during photocatalytic O_2 oxidation of CH_4 on $\text{Au}_{1.0}\text{Fe}_{0.33}\text{-ZnO}$. Other reaction conditions are given in Fig. 2.

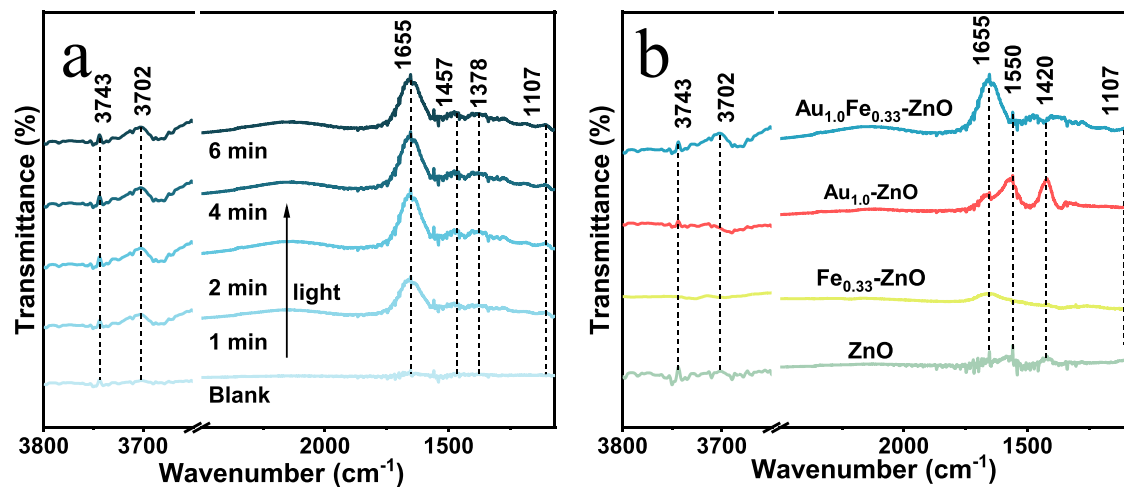


Fig. 5. In situ FT-IR spectra on (a) Au_{1.0}Fe_{0.33}-ZnO with the increasing time of Xe lamp irradiation, (b) Au_{1.0}Fe_{0.33}-ZnO, Au_{1.0}-ZnO, Fe_{0.33}-ZnO, and ZnO after 6 min of Xe lamp irradiation.

to the increase in both the activity and the selectivity due to the enhanced production of •CH₃ and the suppressed formation of CH₃OOH by product. However, a further increase in the CH₄ pressure above 18 bar caused an abrupt decrease in CH₃OH selectivity since excess •CH₃ was produced, which could react with O₂• to produce CH₃OOH and HCHO byproducts. Fig. 4b confirmed that no products were detected in the absence of O₂, suggesting that the CH₄ was only oxidized by molecular O₂ under present reaction conditions. The increase of O₂ pressure caused a rapid increase of CH₃OH yield, which could be mainly attributed to the enhanced activity owing to the rapid production of H₂O₂ into •OH radicals, which could also account for the high CH₃OH selectivity up to 90.7%. However, further increasing O₂ pressure above 2.0 bar resulted in an abrupt decrease in the CH₃OH selectivity due to the rapid formation of O₂• radicals, followed by reacting with •CH₃ to produce CH₃OOH, HCHO, HCOOH, CO, and CO₂ byproducts due to the deep oxidation.

The influence of other factors on the efficiency of photocatalytic CH₄ oxidation on the Au_{1.0}Fe_{0.33}-ZnO was also investigated (see Table S3). No products were detected when the reaction was performed under visible light irradiation or in the presence of H₂O₂ and O₂ without light irradiation. With the increase of Au nanoparticle size from 4.7 nm to 14.6 and 30.7 nm on the Au_{1.0}Fe_{0.33}-ZnO, the CH₃OH yield and selectivity decreased abruptly, suggesting that the enhanced Au nanoparticle size decreased the activity, which could be easily understood by considering the decreased number of Au active sites.

The influences of reaction time, reaction temperature, and the amount of photocatalyst on the performance of photocatalytic CH₄ oxidation over the Au_{1.0}Fe_{0.33}-ZnO were also investigated (see Fig. S8). With the increase of reaction time to 60 from 20 min, the CH₃OH yield and the CH₃OH selectivity remained almost unchanged, obviously owing to the low CH₃OH yield and almost no over oxidation. This could be further confirmed that the CH₃OH yield per min was nearly the same from 0 to 40 min, but gradually decreased from 40 to 60 min. Further increase in the reaction time resulted in the abrupt decrease in the CH₃OH selectivity due to the deep oxidation to produce CH₃OOH, HCHO and CO₂ byproducts, corresponding to the rapid decrease in the CH₃OH yield per min, though that only slight decrease in the total CH₃OH yield was observed. Similarly, with the increase of the reaction temperature to 20°C, the CH₃OH yield increased owing to the enhanced reaction rate since the selectivity remained almost constant. Further increase in the reaction temperature resulted in a rapid decrease in the CH₃OH yield due to the rapid decrease in the CH₃OH selectivity since various byproducts like CH₃OOH, HCHO and CO₂ etc. appeared by over-oxidation. Interestingly, when the amount of photocatalyst increased

from 20 to 40 mg, the CH₃OH selectivity increased rapidly up to 90.7%, but the CH₃OH yield slightly decreased. A possible reason was that the increase of photocatalyst might shield the light irradiation efficiency, which slowed the photocatalytic CH₄ oxidation by O₂ but also retarded the deep oxidation reactions. Further increase in photocatalyst amount caused a significant decrease in both the CH₃OH yield and the CH₃OH selectivity, possibly due to the low photocatalytic reaction rate for CH₄ oxidation and the deep oxidation of CH₃OH by Fenton-like reactions.

3.3. Mechanism investigation

We further performed in situ FT-IR studies under light illumination to gain more insights into the photocatalytic oxidation process of CH₄ by O₂. A mixture gas of CH₄/O₂ was bubbled through deionized water to bring the saturated water vapor into the reaction cell. Background spectra were obtained by flowing through the reactor cell with Ar at 160°C for 15 min, followed by passing mixed gas containing 15 mL/min CH₄ and 5 mL/min O₂ into the reaction system at 20°C for another 40 min without light irradiation. As shown in Fig. 5a, in comparison with the Au_{1.0}Fe_{0.33}-ZnO before light irradiation, it displayed two new peaks at 3743 and 3702 cm⁻¹ indicative of the hydroxyl group [39,40] and another three peaks at 1107, 1378, 1655 cm⁻¹ characteristic of *CH₃O, *CH₂O, *OH₂ [41,42], where the symbol * refers to the radicals detected on the photocatalyst surface rather than the radicals present in the reaction which were marked with •. The intensity of *OH₂ peak increased gradually with increasing irradiation time, which could be attributed to the following reaction: •OH + CH₄ → *OH₂ + •CH₃ [43]. Fig. 5b shows the FT-IR spectra of different photocatalysts after light irradiation for 6 min. Different from that observed on the Au_{1.0}Fe_{0.33}-ZnO, a new peak at 1550 cm⁻¹ was found on either the Au_{1.0}-ZnO or the ZnO, corresponding to *C-O, which had been proved to be a key intermediate for overoxidation of CH₄ [32]. Meanwhile, a strong peak at 1420 cm⁻¹ indicative of *CH₃ appeared, together with a weak peak at 1655 cm⁻¹ characteristic of *OH₂, indicating that photo-induced holes played a dominant role in generating •CH₃ instead of •OH radicals. After loading Fe species on ZnO, the peak characteristic of *CH₃ disappeared, which could be attributed to its reaction with •OH radicals.

The electron paramagnetic resonance (EPR) spectra (Fig. S9) displayed four-peak signals with a 1: 2: 2: 1 line shape, which proved the presence of •OH. As shown in Fig. S9a, the Au_{1.0}Fe_{0.33}-ZnO exhibited low intensity of •OH signal in the presence of Ar. Since in the absence of O₂, no H₂O₂ could be produced by photocatalytic reactions. So, the •OH radicals were mainly generated from H₂O oxidation by photo-induced

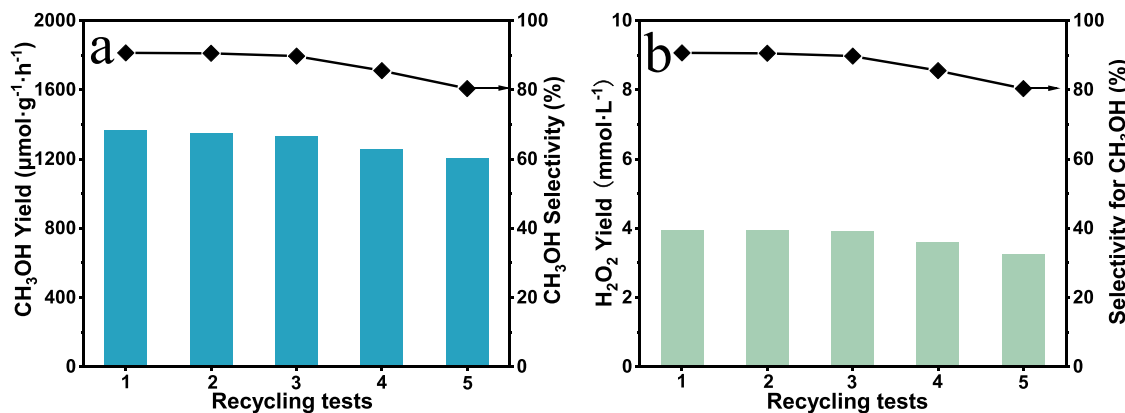


Fig. 6. (a) CH₃OH yield and (b) H₂O₂ yield during recycling tests of the Au_{1.0}Fe_{0.33}-ZnO photocatalyst. Reaction conditions are given in Fig. 2.

holes. By using O₂ instead of Ar, the Au_{1.0}Fe_{0.33}-ZnO exhibited much stronger intensity of •OH signal, obviously owing to the rapid generation of H₂O₂ from O₂ reduction by photocatalytic reactions, which subsequently transformed into •OH radicals through H₂O₂ activation by Fe²⁺ species. By using CH₄ atmosphere, even no significant •OH signals were observed, since the as-produced •OH could rapidly react with •CH₃ to produce CH₃OH product. We further compared the intensity of •OH signal over ZnO, Au_{1.0}-ZnO, Fe_{0.33}-ZnO, and Au_{1.0}Fe_{0.33}-ZnO in O₂ atmospheres under light irradiation for 6 min (see Fig. S9b). The Au_{1.0}Fe_{0.33}-ZnO and Au_{1.0}-ZnO exhibited a much stronger intensity of •OH signal than Fe_{0.33}-ZnO and ZnO, obviously owing to the presence of Au over catalysts. Furthermore, trapping experiments were also performed by using Na₂C₂O₄, K₂Cr₂O₇, salicylic acid, and para-quinone as scavengers for trapping h⁺, e⁻, •OH and O₂• during photocatalytic oxidation of CH₄ on Au_{1.0}Fe_{0.33}-ZnO (see Fig. S10). It could be seen that trapping h⁺ had little influence on the CH₃OH yield. However, trapping •OH could almost completely inhibit the CH₃OH production due to the absence of the reaction between •CH₃ and •OH. Similarly, trapping e⁻ and O₂• also completely inhibited the CH₃OH production since no H₂O₂ was generated from photocatalytic reactions, and thus no •OH radicals could be efficiently produced.

3.4. Durability

The Au_{1.0}Fe_{0.33}-ZnO photocatalyst exhibited both high activity and selectivity, leading to a high CH₃OH yield. Besides, the photocatalyst stability was also an essential criterion for the practical application. Fig. 6a and Fig. 6b show the CH₃OH and H₂O₂ yield during recycling tests of Au_{1.0}Fe_{0.33}-ZnO photocatalyst during selective oxidation of CH₄ to CH₃OH using O₂. Only a slight decrease in either the CH₃OH and H₂O₂ yield or the CH₃OH selectivity was found after 5 cycles, suggesting the excellent durability of the Au_{1.0}Fe_{0.33}-ZnO. The ICP analysis demonstrated the Au-content and Fe-content remained almost unchanged, indicating no significant Au and Fe were leached off from the ZnO support during the reactions owing to the strong interaction between the Au and the Fe species with the ZnO support. Meanwhile, it was confirmed that the Au_{1.0}Fe_{0.33}-ZnO, after being used repetitively for 5 cycles displayed almost the same XPS spectra, XRD patterns, and TEM images as those found in the original Au_{1.0}Fe_{0.33}-ZnO (Fig. S11), corresponding to the similar electronic states, crystal structure, Au_{1.0}Fe_{0.33}-ZnO morphology, Au nanoparticle size, and dispersion state. The slight decrease in the photocatalytic efficiency could be mainly attributed to the leaching of Au_{1.0}Fe_{0.33}-ZnO during the separating and washing process.

4. Conclusion

This work developed a bifunctional photocatalyst (AuFe-ZnO) by uniformly depositing Au nanoparticles and Fe species onto ZnO, which exhibited very high CH₃OH yield and selectivity during photocatalytic O₂ oxidation of CH₄ to CH₃OH under mild conditions. The Au promoted the photocatalytic activity of the ZnO, leading to the efficient production of H₂O₂ from O₂ and activation of CH₄ to •CH₃ radicals. Meanwhile, the Fe²⁺ activated H₂O₂ into •OH radicals, followed by reacting with •CH₃ to produce CH₃OH. The as-resulted Fe³⁺ could be reduced by photoelectrons, leading to the recycling Fenton-like reactions. The cascade photocatalytic Fenton-like reactions and synergistic effects of Au, Fe, and ZnO greatly enhanced the activity and selectivity, leading to the CH₃OH yield of 1365 μmol·g⁻¹·h⁻¹ with high CH₃OH selectivity of up to 90.7%. Meanwhile, the AuFe-ZnO also displayed excellent durability, showing good potential in industrial applications.

CRediT authorship contribution statement

Haoran Du: Data curation, Formal analysis, Investigation, Writing – original draft. **Xiuping Li:** Data curation, Formal analysis. **Zhiyang Cao:** Data curation, Formal analysis. **Shao Zhang:** Data curation, Formal analysis. **Wenzhao Yu:** Data curation, Formal analysis. **Fengyu Sun:** Data curation, Formal analysis. **Shengyao Wang:** Data curation, Formal analysis. **Jingjing Zhao:** Formal analysis, Review. **Jiaqi Wang:** Data curation. **Yuan Bai:** Formal analysis. **Juanjuan Yang:** Data curation, Formal analysis. **Ping Yang:** Data curation, Formal analysis. **Bo Jiang:** Data curation, Formal analysis, Writing – review & editing. **Hexing Li:** Conceptualization, Funding acquisition, Supervision, Writing – review & editing.

Declaration of Competing Interest

The authors declare that they have no known competing financial interests or personal relationships that could have appeared to influence the work reported in this paper.

Data Availability

No data was used for the research described in the article.

Acknowledgment

This work was supported by the National Key Research and Development Program of China (2020YFA0211004), the National Natural

Science Foundation of China (22236005, 22106106), Shanghai Government (22dz1205400, 21ZR1446600).

Appendix A. Supporting information

Supplementary data associated with this article can be found in the online version at doi:10.1016/j.apcatb.2022.122291.

References

- [1] L. Yuliati, H. Yoshida, Photocatalytic conversion of methane, *Chem. Soc. Rev.* 37 (2008) 1592–1602.
- [2] D. Saha, H.A. Grappe, A. Chakraborty, G. Orkoulas, Postextraction separation, on-board storage, and catalytic conversion of methane in natural gas: a review, *Chem. Rev.* 116 (2016) 11436–11499.
- [3] M. Ravi, M. Ranocchiaro, J.A. van Bokhoven, The direct catalytic oxidation of methane to methanol—a critical assessment, *Angew. Chem. Int. Ed.* 56 (2017) 16464–16483.
- [4] A.I. Olivos-Suarez, Á. Szécsényi, E.J.M. Hensen, J. Ruiz-Martinez, E.A. Pidko, J. Gascon, Strategies for the direct catalytic valorization of methane using heterogeneous catalysis: challenges and opportunities, *ACS Catal.* 6 (2016) 2965–2981.
- [5] A.A. Latimer, A. Kakekhani, A.R. Kulkarni, J.K. Nørskov, Direct methane to methanol: the selectivity–conversion limit and design strategies, *ACS Catal.* 8 (2018) 6894–6907.
- [6] R. Jin, M. Peng, A. Li, Y. Deng, Z. Jia, F. Huang, Y. Ling, F. Yang, H. Fu, J. Xie, X. Han, D. Xiao, Z. Jiang, H. Liu, D. Ma, Low temperature oxidation of ethane to oxygenates by oxygen over iridium-cluster catalysts, *J. Am. Chem. Soc.* 141 (2019) 18921–18925.
- [7] H. Zhang, C. Li, Q. Lu, M.J. Cheng, W.A. Goddard 3rd, Selective activation of propane using intermediates generated during water oxidation, *J. Am. Chem. Soc.* 143 (2021) 3967–3974.
- [8] M.C. Simons, S.D. Prinslow, M. Babucci, A.S. Hoffman, J. Hong, J.G. Vitillo, S. R. Bare, B.C. Gates, C.C. Lu, L. Gagliardi, A. Bhan, Beyond radical rebound: methane oxidation to methanol catalyzed by iron species in metal-organic framework nodes, *J. Am. Chem. Soc.* 143 (2021) 12165–12174.
- [9] N. Agarwal, S.J. Freakley, R.U. McVicker, S.M. Althahban, N. Dimitratos, Q. He, D. J. Morgan, R.L. Jenkins, D.J. Willock, S.H. Taylor, C.J. Kiely, G.J. Hutchings, Aqueous Au-Pd colloids catalyze selective CH₄ oxidation to CH₃OH with O₂ under mild conditions, *Science* 358 (2017) 223–227.
- [10] X. Wu, Y. Zeng, H. Liu, J. Zhao, T. Zhang, S.L. Wang, Noble-metal-free dye-sensitized selective oxidation of methane to methanol with green light (550 nm), *Nano Res.* 14 (2021) 4584–4590.
- [11] L. Luo, J. Luo, H. Li, F. Ren, Y. Zhang, A. Liu, W.X. Li, J. Zeng, Water enables mild oxidation of methane to methanol on gold single-atom catalysts, *Nat. Commun.* 12 (2021) 1218–1224.
- [12] S. Grundner, M.A. Markovits, G. Li, M. Tromp, E.A. Pidko, E.J. Hensen, A. Jentys, M. Sanchez-Sanchez, J.A. Lercher, Single-site trinuclear copper oxygen clusters in mordenite for selective conversion of methane to methanol, *Nat. Commun.* 6 (2015) 7546–7552.
- [13] J. Shan, M. Li, L.F. Allard, S. Lee, M. Flytzani-Stephanopoulos, Mild oxidation of methane to methanol or acetic acid on supported isolated rhodium catalysts, *Nature* 551 (2017) 605–608.
- [14] H. Song, X. Meng, Z.-j Wang, H. Liu, J. Ye, Solar-energy-mediated methane conversion, *Joule* 3 (2019) 1606–1636.
- [15] I. Ghosh, J. Khamrai, A. Savateev, N. Shlapakov, B. Knig, Organic semiconductor photocatalyst can bifunctionalize arenes and heteroarenes, *Science* 365 (2019) 360–366.
- [16] B.H. Lee, S. Park, M. Kim, A.K. Sinha, S.C. Lee, E. Jung, W.J. Chang, K.S. Lee, J. H. Kim, S.P. Cho, H. Kim, K.T. Nam, T. Hyeon, Reversible and cooperative photoactivation of single-atom Cu/TiO₂ photocatalysts, *Nat. Mater.* 18 (2019) 620–626.
- [17] Z. Sun, C. Wang, Y.H. Hu, Highly selective photocatalytic conversion of methane to liquid oxygenates over siliconolybdic-acid/TiO₂ under mild conditions, *J. Mater. Chem. A* 9 (2021) 1713–1719.
- [18] K. Villa, S. Murcia-López, J.R. Morante, T. Andreu, An insight on the role of La in mesoporous WO₃ for the photocatalytic conversion of methane into methanol, *Appl. Catal. B* 187 (2016) 30–36.
- [19] J. Yang, J. Hao, J. Wei, J. Dai, Y. Li, Visible-light-driven selective oxidation of methane to methanol on amorphous FeOOH coupled m-WO₃, *Fuel* 266 (2020) 117104–117110.
- [20] W. Zhou, X. Qiu, Y. Jiang, Y. Fan, S. Wei, D. Han, L. Niu, Z. Tang, Highly selective aerobic oxidation of methane to methanol over gold decorated zinc oxide via photocatalysis, *J. Mater. Chem. A* 8 (2020) 13277–13284.
- [21] J. Xie, R. Jin, A. Li, Y. Bi, Q. Ruan, Y. Deng, Y. Zhang, S. Yao, G. Sankar, D. Ma, J. Tang, Highly selective oxidation of methane to methanol at ambient conditions by titanium dioxide-supported iron species, *Nat. Catal.* 1 (2018) 889–896.
- [22] S. Witzel, A.S.K. Hashmi, J. Xie, Light in gold catalysis, *Chem. Rev.* 121 (2021) 8868–8925.
- [23] R.A. Periana, D.J. Taube, et al., A mercury-catalyzed, high-yield system for the oxidation of methane to methanol, *Science* 5093 (1993) 340–343.
- [24] C. Hammond, M.M. Forde, M.H. Ab Rahim, A. Thetford, Q. He, R.L. Jenkins, N. Dimitratos, J.A. Lopez-Sanchez, N.F. Dummer, D.M. Murphy, A.F. Carley, S. H. Taylor, D.J. Willock, E.E. Stangland, J. Kang, H. Hagen, C.J. Kiely, G. J. Hutchings, Direct catalytic conversion of methane to methanol in an aqueous medium by using copper-promoted Fe-ZSM-5, *Angew. Chem. Int. Ed.* 21 (2012) 5219–5223.
- [25] S. Sun, A.J. Barnes, X. Gong, R.J. Lewis, N.F. Dummer, T. Bere, G. Shaw, N. Richards, D.J. Morgan, G.J. Hutchings, Lanthanum modified Fe-ZSM-5 zeolites for selective methane oxidation with H₂O₂, *Catal. Sci. Technol.* 11 (2021) 8052–8064.
- [26] X.Y. Wu, Z. Tang, X. Zhao, X. Luo, S. John Pennycook, S.L. Wang, Visible-light driven room-temperature coupling of methane to ethane by atomically dispersed Au on WO₃, *J. Energy Chem.* 61 (2021) 195–202.
- [27] N. Feng, H. Lin, H. Song, L. Yang, D. Tang, F. Deng, J. Ye, Efficient and selective photocatalytic CH₄ conversion to CH₃OH with O₂ by controlling overoxidation on TiO₂, *Nat. Commun.* 12 (2021) 4652–4655.
- [28] X. Wu, Q. Zhang, W. Li, B. Qiao, D. Ma, S.L. Wang, Atomic-scale Pd on 2D titania sheets for selective oxidation of methane to methanol, *ACS Catal.* 11 (2021) 14038–14046.
- [29] H. Song, X. Meng, S. Wang, W. Zhou, S. Song, T. Kako, J. Ye, Selective photo-oxidation of methane to methanol with oxygen over dual-cocatalyst-modified titanium dioxide, *ACS Catal.* 10 (2020) 14318–14326.
- [30] L. Luo, Z. Gong, Y. Xu, J. Ma, H. Liu, J. Xing, J. Tang, Binary Au-Cu reaction sites decorated ZnO for selective methane oxidation to Cl oxygenates with nearly 100% selectivity at room temperature, *J. Am. Chem. Soc.* 144 (2022) 740–750.
- [31] H. Song, X. Meng, S. Wang, W. Zhou, X. Wang, T. Kako, J. Ye, Direct and selective photocatalytic oxidation of CH₄ to oxygenates with O₂ on cocatalysts/ZnO at room temperature in water, *J. Am. Chem. Soc.* 141 (2019) 20507–20515.
- [32] S. Zhu, X. Li, Z. Pan, X. Jiao, K. Zheng, L. Li, W. Shao, X. Zu, J. Hu, J. Zhu, Y. Sun, Y. Xie, Efficient photooxidation of methane to liquid oxygenates over ZnO nanosheets at atmospheric pressure and near room temperature, *Nano Lett.* 21 (2021) 4122–4128.
- [33] Y. Zhou, L. Zhang, W. Wang, Direct functionalization of methane into ethanol over copper modified polymeric carbon nitride via photocatalysis, *Nat. Commun.* 10 (2019) 506–509.
- [34] Y. Fan, W. Zhou, X. Qiu, H. Li, Y. Jiang, Z. Sun, D. Han, L. Niu, Z. Tang, Selective photocatalytic oxidation of methane by quantum-sized bismuth vanadate, *Nat. Sustain.* 4 (2021) 509–515.
- [35] Y. Zeng, X. Luo, F. Li, A. Huang, H. Wu, G.Q. Xu, S.L. Wang, Noble metal-free FeOOH/Li_{0.1}WO₃ core-shell nanorods for selective oxidation of methane to methanol with visible-NIR light, *Environ. Sci. Technol.* 55 (2021) 7711–7720.
- [36] J.A. Grossnickle, G.C. Vlases, A.L. Hoffman, P.A. Melnik, R.D. Milroy, A. Tankut, K. M. Velas, Particle and recycling control in translation, confinement, and sustainment upgrade, *Phys. Plasmas* 17 (2010) 32506–32511.
- [37] J. Liu, D. Qian, H. Feng, J. Li, J. Jiang, S. Peng, Y. Liu, Designed synthesis of TiO₂-modified iron oxides on/among carbon nanotubes as a superior lithium-ion storage material, *J. Mater. Chem. A* 2 (2014) 11372–11375.
- [38] N. Ohtsu, A. Nomura, M. Oku, T. Shishido, K. Wagatsuma, X-ray photoelectron spectroscopic studies on oxidation behavior of nickel and iron aluminides under oxygen atmosphere at low pressures, *Appl. Surf. Sci.* 254 (2008) 5336–5341.
- [39] W. Yang, R. Zhang, B. Chen, D. Duprez, S. Royer, New aspects on the mechanism of C₃H₆ selective catalytic reduction of NO in the presence of O₂ over LaFe_{1-x}(Cu, Pd)_xO₃-delta perovskites, *Environ. Sci. Technol.* 46 (2012) 11280–11288.
- [40] L. Zhao, Y. Zhang, S. Bi, Q. Liu, Metal-organic framework-derived CeO₂-ZnO catalysts for C₃H₆-SCR of NO: an in situ DRIFTS study, *RSC Adv.* 9 (2019) 19236–19242.
- [41] S. Bai, Y. Xu, P. Wang, Q. Shao, X. Huang, Activating and converting CH₄ to CH₃OH via the CuPdO_x/CuO nanointerface, *ACS Catal.* 9 (2019) 6938–6944.
- [42] K. Zheng, Y. Wu, Z. Hu, X. Jiao, L. Li, Y. Zhao, S. Wang, S. Zhu, W. Liu, W. Yan, Y. Sun, Y. Xie, Selective CH₄ partial photooxidation by positively charged metal clusters anchored on carbon aerogel under mild conditions, *Nano Lett.* 21 (2021) 10368–10376.
- [43] B. Wu, T. Lin, M. Huang, S. Li, J. Li, X. Yu, R. Yang, F. Sun, Z. Jiang, Y. Sun, L. Zhong, Tandem catalysis for selective oxidation of methane to oxygenates using oxygen over PdCu/Zeolite, *Angew. Chem. Int. Ed.* 61 (2022) 416–423.